Double electron-electron resonance with multiple non-selective chirp refocusing

Andrin Doll, Gunnar Jeschke

Supplementary Information

1. Pictorial representations of evolution pathways

In the main text in Section 3.2.1., dipolar modulation formulas of DEER4 and nDEER4 have been provided. Here, we provide a pictorial representation of these evolution pathways and the necessary theory to apply the pictorial analysis to more complicated pathways. In particular, we will make use of this method in Section 6 of this SI, where spurious dipolar evolution pathways are analyzed.

Pictorial representations of evolution due to spin-spin couplings throughout a pulse sequence have been used in a variety of different contexts in magnetic resonance (see for instance [1–3]). In essence, these representations depict the phase of one spin acquired under the coupling to its partner spin. In our context, the coupling Hamiltonian reads

$$\hat{\mathcal{H}}_{dd} = \omega_{12}\hat{S}_{1,z}\hat{S}_{2,z} \qquad (1)$$

where ω_{12} is the coupling strength. Without loss of generality, we consider the phase of spin S_1 due to the coupling to spin S_2. For such a Hamiltonian, it is well known that free evolution for a time interval t_f results in acquisition of a phase

$$\varphi_{dd}(t_f) = \pm\omega_{12}/2 \cdot t_f \qquad (2)$$

Using product operator formalism [4], this is equivalent to

$$\hat{S}_{1,x} \xrightarrow{\varphi_{dd}(2\hat{S}_{1,z}\hat{S}_{2,z})} \hat{S}_{1,x}\cos(\varphi_{dd}) + 2\hat{S}_{1,y}\hat{S}_{2,z}\sin(\varphi_{dd}) \quad (3)$$

if the initial state is created by a $\pi/2$ pulse resonant with the spin S_1, which corresponds to the situation encountered in DEER/nDEER.

The acquisition of phase under the coupling can be controlled by selective refocusing pulses. In particular, selective inversion of either S_1 or S_2 changes the effective sign of $\omega_{12}/2$ in Eq. (2). By following the net phase φ_{dd} throughout the pulse sequence, the evolution under the coupling can be quantified. Of particular relevance are constellations where $\varphi_{dd} = 0$, since the dipolar evolution is refocused at this time instant.

As a first example, we consider the DEER4 and nDEER4 pulse sequences in absence of the pump pulse. The three relevant pulses are shown in black on the top of Fig. S1. The black curves underneath illustrate the temporal evolution of φ_{dd} for selective refocusing in DEER4 and for non-selective refocusing in nDEER4. Notice that each selective refocusing pulse is
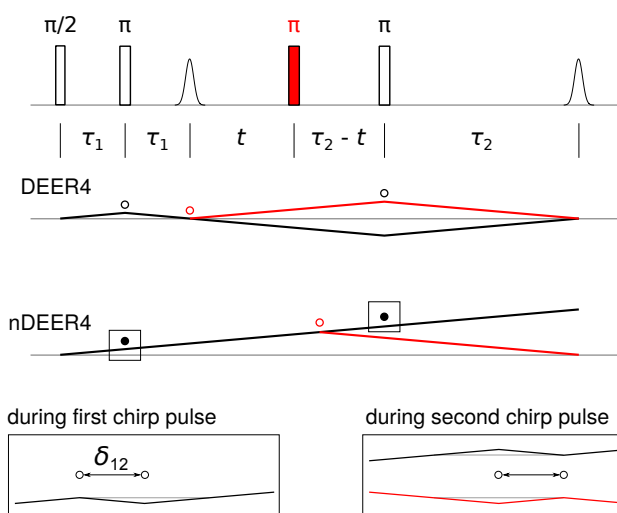

Figure S1: Pictorial representation of dipolar evolution pathways in DEER4 (top) and nDEER4 (bottom). Filled black circles ● denote non-selective refocusing, while empty black circles ○ denote selective refocusing. The evolution pathways in black are obtained in absence of the pump pulse. The red curves branching off are due to the pump pulse with timing indicated by the empty red circle ○. All pathways in red refocus the dipolar evolution at the position of the relevant echo. The two insets on the bottom illustrate the refocusing of a net time interval of duration $2\delta_{12}$ during the frequency-swept refocusing pulses in nDEER4. In this case, δ_{12} is the delay that passes between inversion of the first and the second spin. This effect is specific to frequency-swept refocusing pulses and is analyzed in further detail in Section 2 of this SI.

indicated by an empty black circle ○, while each non-selective refocusing pulse is indicated by a filled black circle ●. As is readily seen, the evolution with selective refocusing is refocused at the position of the relevant DEER4 echo, while the evolution with non-selective refocusing is not refocused at all and evolves throughout $2(\tau_1 + \tau_2)$. These pathways constitute the unmodulated DEER4/nDEER4 contribution and the mathematical equivalent is provided in Eqs. (4) and (5) in the main text.

The pump pulse in DEER4/nDEER4 has variable timing parametrized by t. Using the pictorial representation, the zero time t_0 of the pump pulse that refocuses the dipolar evolution can be obtained by a geometrical construction (using an axono-

metric grid). In particular, one can literally draw the evolution pathway starting from the desired target point at the position of the relevant echo. The initial curvature of this back-evolution has to be opposite to the curvature of φ_{dd} in the absence of the pump pulse. In doing so, the backward evolution eventually crosses the forward evolution and this crossing point corresponds to the zero time t_0.

In Fig. S1, these backward evolution pathways are shown in red. The resulting crossing point t_0 is indicated by the red circle ○. By making use of Eq. (3), it can be readily shown that knowledge of t_0 allows to write down the modulation formula for coherence at the time instant where the pulse sequence refocuses the Zeeman interaction by echo formation. In particular,

$$\left\langle \hat{S}_{1,x} \right\rangle (t) = \cos(\omega_{12} \cdot (t - t_0)) \tag{4}$$

With the zero times t_0 obtained geometrically, we therefore arrive at Eqs. (2) and (3) in the main text. Notice that the times t_0 have to be determined with respect to origin of t.

Besides the t_0 times, the geometrical approach also reveals the range of t within which Eq. (4) above is valid. In particular, a non-selective refocusing pulse does not affect the dipolar evolution so that this pulse can be neglected when deriving the modulation formula. In this viewpoint, the nDEER4 sequence consists of one single selective inversion pulse with variable timing t and zero time at $t_0 = \tau_2 - \tau_1$, while the sole purpose of the non-selective inversion pulses is to refocus the Zeeman interaction[1]. Accordingly, the pump pulse can be placed at any time instant within the pulse sequence. In particular, the pump pulse can be moved ahead of the first refocusing pulse down to $t = -2\tau_1$. The nDEER4 modulation formula is thus valid for $-2\tau_1 < t < 2\tau_2$. The effective phase φ_{dd} acquired under the dipolar coupling can therefore be varied from $\varphi_{dd} = 0$ to $\varphi_{dd} = (\tau_1 + \tau_2) \cdot \omega_{12}$.

This is not the case for the DEER4 modulation formula, since the selective refocusing pulses do influence the dipolar phase φ_{dd}. In particular, the modulation formula looses validity if the pump pulse is skipping any of the selective refocusing pulses. Accordingly, the DEER4 modulation formula is valid for $-\tau_1 < t < \tau_2$. The effective phase φ_{dd} acquired under the dipolar coupling can therefore be varied from $\varphi_{dd} = 0$ to $\varphi_{dd} = \tau_2 \cdot \omega_{12}$, which is smaller than for nDEER4.

The range over which the corresponding modulation formula is valid can readily be identified in the pictorial representation. Essentially, the pump pulse can be displaced from t_0 indicated by the red dot ○ until it eventually reaches a selective refocusing pulse labeled by ○. This aspect is important to keep in mind in Section 6 of this SI, where a number of pathways in CP2-nDEER and CP4-nDEER will be analyzed using the geometrical approach described here.

---

[1]This actually establishes a conceptual link between nDEER and other experiments that employ non-selective refocusing pulses to refocus the Zeeman interaction, while leaving the dipolar evolution unaffected. Such experiments include SIFTER [5] and DQC experiments [6]. Nevertheless, the spin dynamics in these experiments is different than in nDEER. Moreover, pulse skipping as implemented in CP2-nDEER and CP4-nDEER is a unique capability of nDEER and could not be implemented in the other techniques without altering the spin dynamics.

Notice that in Fig. S1, the insets at the bottom depict the dipolar evolution during the chirp refocusing pulses in nDEER4. In particular, each chirp pulse inverts the two spins sequentially with a short delay δ_{12} in-between, so that it does not correspond to a strict non-selective refocusing pulse. As can be inferred from the insets, these sequential selective inversions refocus the dipolar evolution over a time interval $2\delta_{12}$, which corresponds to a loss of $\omega_{12}\delta_{12}$ in φ_{dd}. Since the slope of the defocusing pathway (black) and of the refocusing pathway (red) is opposite, the phase loss by each pulse is compensated in nDEER4. The actual distribution of this delay δ_{12} is further analyzed below in the next section.

2. Rationale for *non-selective* chirp refocusing

This section provides details on the calculation of the delay δ_{12} between the consecutive inversion of two coupled spins during a frequency-swept refocusing pulse. This delay has already been analyzed for the case that the frequency-swept pulse excites two coupled spins that are distributed according to the nitroxide spectrum [7, 8]. In the nDEER experiment, however, the two spins that are inverted have a distinct spectral distribution related to the observer spins A and to the pump spins B. For the calculation of δ_{12}, the distribution of the A and B spins thus needs to be determined.

The spectral distribution of the A and the B spins was based on the experimental data presented in Fig. 2b in the main text. In particular, the excitation profiles of the pulses as well as the spectral line shape were determined experimentally. The nitroxide spectrum is illustrated in black in Fig. S2a. The spectral distribution of the B spins shown in orange was obtained by multiplication of the spectrum with the excitation profile p_{pump} of the pump pulse. For the spectral distribution of the A spins, several additional aspects needed to be taken into consideration. First, the excitation profiles of the $\pi/2$ excitation pulse p_{obs} and the pump pulse p_{pump} had spectral overlap. If the pump pulse excites A spins, there is no longer a contribution to the echo of interest. In order to exclude these, the distribution of A spins was obtained by multiplication of the nitroxide spectrum by $p_{obs} \cdot (1 - p_{pump})$. As a second aspect, only the spectral range over which the spin echo was integrated was considered. Outside this range, the distribution of the A spins was set to zero. The resulting distribution is shown in red in Fig. S2a.

Given the A and B spins' distribution, timings can be deduced based on the instantaneous frequency of the refocusing pulse. The frequency-time profile of the bandwidth-compensated pulse utilized in the experiments is illustrated by the gray curve in Fig. S2a, where the ordinate represents a normalized time axis. In panel b, the resulting distributions of δ_A and δ_B are indicated. These denote the times when the frequency-swept pulse is resonant with the A and B spin packets. In essence, the distributions of δ_A and δ_B are projections of the spectral distributions onto the non-linear time-frequency relation of the refocusing pulse.

Given the distributions p_{δ_A} and p_{δ_B} of the δ_A and δ_B times, the distribution $p_{\delta_{12}}$ of the delay δ_{12} between two consecutive in-
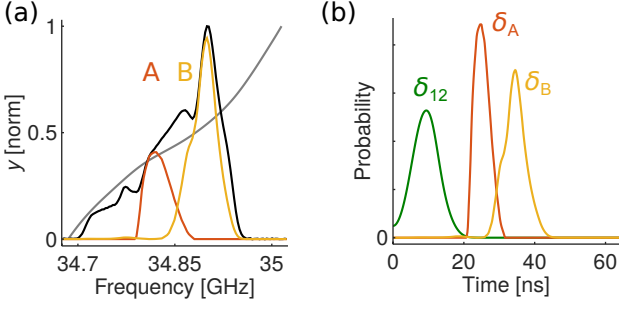
Figure S2: Distribution of time δ_{12} between frequency-progressive selective chirp refocusing. **(a)** Nitroxide spectrum (black) cast to a frequency axis and spin packets A and B that contribute to the relevant dynamics (red and orange). The gray curve represents the frequency modulation function of the 64 ns long chirp refocusing pulse with $\Delta f = 330$ MHz. The instantaneous frequency is along the abscissa and the ordinate here represents a normalized time axis. **(b)** Distributions of δ_A and δ_B, which are the timings when the chirp pulse is resonant with the A and B spins, respectively. The green curve is the distribution of the delay δ_{12}, which is the delay between δ_A and δ_B times.

versions can be calculated. In particular,

$$p_{\delta_{12}} = p_{\delta_1} \cdot p_{\delta_2} |_{\delta_2 - \delta_1 = \delta_{12}} \tag{5}$$

which is readily calculated by formation of a histogram. Notice that this calculation needs to be done twice. Once for $p_{\delta_1} = p_{\delta_A}$ and $p_{\delta_2} = p_{\delta_B}$, and once for $p_{\delta_1} = p_{\delta_B}$ and $p_{\delta_2} = p_{\delta_A}$. This is because there is a non-zero probability that the B spin is inverted before the A spin. For the majority of cases, however, the B spin is inverted after the A spin. If the A and the B spins would have the same spectral distribution, we would obtain the same distribution independent on which spin is excited first. This situation formally corresponds to the case discussed for SIFTER [8].

The distribution of δ_{12} that results from this analysis is shown in green in panel b. This distribution represents a bell-shaped peak centered at 10 ns. The overall spread is on the order of 20 ns. As discussed in the main text and illustrated above in the bottom inset in Fig S1, this delay refocuses the dipolar evolution over a total period of $2\delta_{12}$. For multiple refocusing pulses as encountered in nDEER, each pulse adds such refocusing over $2\delta_{12}$. By means of inversion of the coupling Hamiltonian by the selective pump pulse, interference by the distribution of δ_{12} can be avoided by compensation. The nDEER4 modulation is thus not affected by δ_{12} (see Fig. S1 and Section 3.2.3 in the main text). In CP2-nDEER, however, the dipolar refocusing by the pump pulse does no longer compensate δ_{12} after pulse skipping. As a consequence, a phase of $2\omega_{12}\delta_{12}$ needs to be subtracted in the phase argument of the modulation formulas after a pulse skip. For CP2-nDEER, this results in an overall spread in the time axis t by 40 ns. This spread is certainly smaller than the spread introduced by a 48 ns long chirp pump pulse examined previously in DEER4 [9]. Accordingly, we would expect that CP2-nDEER4 at the experimental performance demonstrated in this study allows for faithful analysis of distances down to 2 nm. This corresponds to a distance range that is shorter than

what is accessible by the constrained time increment Δt of 96 ns.

For CP4-nDEER, there are four refocusing pulses, which enhances the overall spread to 80 ns upon the second pulse skip. In principle, this comes close to the minimum time increment Δt of 96 ns. However, this enhanced uncertainty applies only for the last quarter of the acquired time window. In many situations, this last part of the dipolar modulation has already decayed to a small value due to the conformational distribution of the two spin labels.

Overall, the spread in δ_{12} for nDEER techniques is small with respect to the dipolar couplings of interest. Under this condition, we can consider the chirp refocusing pulses used in our experiments to be non-selective refocusing pulses. Clearly, if such experiments are performed on a spectrometer that does not achieve the performance of our home-built spectrometer, the analysis described above needs to be repeated to estimate the range of distances accessible by the technique.

3. General modulation formula

In the following, we provide a modulation formula that is more general than the formulas presented in the main text. In particular, we consider a spin system where the observer spin S_A is weakly coupled to N spins S_{Bi}, where $i = 1...N$. The Hamiltonian is given as

$$\hat{\mathcal{H}}_0 = \Omega_A \hat{S}_{A,z} + \sum_{i=1}^{N} \Omega_{Bi} \hat{S}_{Bi,z} + \sum_{i=1}^{N} \omega_i \hat{S}_{A,z} \hat{S}_{Bi,z} \tag{6}$$

where Ω_A and Ω_{Bi} are the resonance offsets and ω_i are the secular dipolar couplings. Notice that for ease of analysis, pseudo-secular contributions to the dipole-dipole interaction are neglected. Moreover, there is no need to consider the dipolar couplings between the B_i spins, since these do not contribute to the spin dynamics for the static *relaxation-free* treatment here.

To write down the modulation formula, we consider, for each coupling partner B_i, two dipolar evolution pathways, namely whether or not the coupled spin B_i is inverted or not by the pump pulse. To weight these two pathways, p_i denotes the inversion probability. DEER and nDEER have in common that a non-inverted partner spin contributes by an unmodulated constant $c(\omega_i)$, while an inverted parter spin contributes with a modulation by $m(\omega_i, t)$. For the two experiments, the contributions are

	$c(\omega_i)$	$m(\omega_i, t)$
DEER	1.0	$\cos(\omega_i \cdot t)$
nDEER	$\cos(\omega_i \cdot \tau_{sum})$	$\cos(\omega_i \cdot (t - \tau_2 + \tau_1))$

$$\tag{7}$$

where $\tau_{sum} = \tau_1 + \tau_2$. Using these contributions and the flip probability p_i, the echo is modulated according to

$$V(t) = \left\langle \prod_i \left\{ (1 - p_i) \cdot c(\omega_i) + p_i \cdot m(\omega_i, t) \right\} \right\rangle \tag{8}$$

where the brackets indicate ensemble averaging over all observed A spins. In general, each A spin has different p_i and

ω_i that depend on the spatial arrangement of the B spins around the A spin.

To further simplify the modulation formula, the correlations amongst the p_i and ω_i values need to be taken into consideration. In particular, there is rarely a correlation between inter-molecular and intra-molecular contributions for spin-labeled macromolecules embedded into disordered solids. Accordingly, these contributions can be averaged separately, such that

$$V(t) = \left\langle \prod_{i\,\text{intra}} \left\{ (1 - p_i) \cdot c(\omega_i) + p_i \cdot m(\omega_i, t) \right\} \right\rangle$$
$$\cdot \left\langle \prod_{i\,\text{inter}} \left\{ (1 - p_i) \cdot c(\omega_i) + p_i \cdot m(\omega_i, t) \right\} \right\rangle \tag{9}$$

$$= F(t) \cdot B(t) \tag{10}$$

where $F(t)$ contains the intra-molecular and $B(t)$ the inter-molecular contribution.

Ensemble averaging of the intra-molecular contribution $F(t)$ can be further simplified, provided that certain conditions are fulfilled. As a first condition, we note that the correlation between p_i and ω_i corresponds to correlations between the dispersion of resonance offsets Ω_{Bi} and dipolar couplings ω_i. Since the dispersion of Ω_{Bi}, the spectrum, encodes the orientation of the spin (with respect to the applied field), and ω_i encodes the orientation of the spin-spin vector, correlations between p_i and ω_i indicate a rigid mutual spin-spin geometry [10]. If such geometrical correlations can be neglected, p_i and ω_i can be averaged separately. The second condition that allows simplification of $F(t)$ is related to the number of intra-molecular spin partners. In many practical cases, there is only one intra-molecular partner and $F(t)$ is no longer a product over multiple contributions.

If orientational correlations are neglected and only one spin partner is present, $F(t)$ reduces to Eqs. (6) and (7) in the main text. The main difference in $F(t)$ between DEER and nDEER is that the unmodulated contributions in nDEER are suppressed due to dephasing over τ_{sum}, which we refer to as dipolar attenuation and whose consequences have been considered in the main text.

Ensemble averaging of the inter-molecular contribution $B(t)$ has been extensively studied for DEER [11, 12]. In particular, the inter-molecular contribution is often well described by

$$B_{\text{DEER}}(t) = \exp(-kt)^{d/3} \tag{11}$$

where d is the background dimensionality and k is a decay parameter. In DEER, the parameters d and k can be extracted from experimental data if the time window is of sufficient duration for the modulation in $F(t)$ to decay to zero [13].

The background contribution of nDEER is in general not the same as for DEER due to dipolar attenuation. However, dipolar attenuation within $B(t)$ is weak for dilute samples as encountered in this study. In particular, the unmodulated contributions $c(\omega_i)$ to $B(t)$ are close to 1.0, since the long distances related to inter-molecular spin partners rarely evolve beyond their dipolar oscillation period. At low molecular concentrations, we can therefore assume

$$B_{\text{nDEER}}(t) \approx B_{\text{DEER}}(t - \tau_2 + \tau_1) \tag{12}$$

Experimental evidence for this approximation is provided below in Section 4 of this SI.

While the inter-molecular contribution $B(t)$ is almost identical for nDEER and DEER, it is worth to reconsider the suppressed background decay in nDEER. As stated in the main text, the apparent background curvature that is directly visible in experimental data is the product between the constant intra-molecular contribution and $B(t)$. The less apparent contribution of $B(t)$ is that it also multiplies to the dipolar modulation. In general, the latter contribution results in broadening of the dipolar spectrum, since $B(t)$ results in a faster decay of the dipolar modulation.

In DEER, this less apparent contribution can be removed by division by $B(t)$, which can be extracted from the curvature in the experimental data. In nDEER, however, the background curvature that is directly visible in experimental data is largely suppressed by dipolar attenuation. The actual shape of $B(t)$ is therefore difficult to retrieve from experimental data. In particular, extraction of $B(t)$ from nDEER data would require a quantification of $c(\omega_i)$ as well as a quantification of the modulation depth λ and the labeling efficiency. In fact, we expect the labeling efficiency to be of particular relevance for the experimental nDEER background curvature. For the long acquisition times t in our experiments, the intra-molecular modulation has decayed considerably at τ_{sum}. One would therefore expect almost complete suppression of the apparent background curvature by dipolar attenuation. The apparent background curvature observed in our nDEER experiments is therefore likely to origin from other pathways than the two dipolar evolution pathways that have been considered in the modulation formula derived here. These other pathways include contributions from molecules where the intra-molecular spin partner is not attached due to the labeling efficiency. As already mentioned in the main text, there is no dipolar attenuation for singly-labeled molecules, such that molecules with incomplete labeling contribute to the background curvature by $B(t)$.

These aspects make it difficult to extract $B(t)$ in nDEER and use it to correct the apparent dipolar modulation for broadening by $B(t)$. In particular, the background decay $B_{\text{exp}}(t)$ extracted from experimental data is less pronounced than the actual $B(t)$, so that the broadening by $B(t)$ is only partially removed by dividing experimental nDEER data by $B_{\text{exp}}(t)$.

This incomplete background deconvolution determines the scope of nDEER. In particular, a faithful reconstruction of the intra-molecular dipolar spectrum is possible if the intra-molecular modulation decays faster than the background contribution $B(t)$. One would therefore expect a limitation for samples where a fast background decay $B(t)$ is paired with a slow and extended intra-molecular modulation. Samples with rigid conformations should therefore not be measured at too high concentration. Accordingly, nDEER is a technique dedicated to macromolecules at low concentrations, as for instance the system examined in this study.

Notice that when working in the regime where $B(t)$ introduces no considerable broadening, DEER and nDEER form factors can be extracted from experimental data by subtraction of the apparent background. As opposed to the division by $B(t)$, which reduces broadening of dipolar spectra, background subtraction

does not enhance noise towards the end of $F(t)$. The scope of nDEER can therefore be examined by testing existing DEER data for coincidence when either dividing or subtracting experimental data by the background curvature.

4. Dipolar attenuation within the inter-molecular background

In order to obtain insight into dipolar attenuation within the nDEER background decay $B(t)$, DEER4 and nDEER4 was performed with a solution of 500 μM TEMPOL, which has been dissolved in a water-glycerol solution (1:1 in volume). Due to the presence of water protons, the phase memory time T_m for this solution was shorter than for the biradical investigated in the main text. The available time window for dipolar evolution was therefore reduced. The shorter time window is the reason why we selected a large concentration of 500 μM to study dipolar attenuation within $B(t)$.
Experimental results are shown in Fig. S3, where DEER4 (orange) and nDEER4 (blue) data were recorded using either τ_2 = 2.5 μs (dotted) or τ_2 = 4 μs (solid). In panel a, the curves are normalized to the maximum amplitude of the DEER4 trace. As is readily seen, the decay of the DEER4 curves is identical, whereas the nDEER4 decays have a smaller relative amplitude. The largest relative attenuation was observed for the nDEER4 trace with the longer τ_2 setting. Note that in order to reduce effects related to the different bandwidths of the nDEER4 and DEER4 echo, we here only considered spin packets at the observation frequency.
In panel b, all curves were normalized by their maximum value. As is seen in this representation, the shape of the decay was not altered considerably when changing from DEER4 to nDEER4. These experimental results are explained by dipolar attenuation. In particular, dipolar attenuation is enhanced when prolonging τ_2, since the coupled spins dephase over a longer time period τ_{sum}. This is especially relevant for the case here, where the modulation by the stochastically distributed spin partners is a monotonous decay function.
The fact that the shape of the decay was not altered significantly when changing from DEER4 to nDEER4 reveals that there is no significant filtering effect for the case here. In particular, each observer spin is coupled to multiple spin partners, such that the net dipolar attenuation of a particular pathway is inversely proportional to the number of spin partners flipped by the pump pulse. As discussed in the main text, this filtering effect selects the largest combination product for an intra-molecular multi-spin system. For the case here, dephasing over τ_{sum} is too weak to result in considerable filtering. Nevertheless, it is presumed that such effects can be observed at larger spin concentrations and larger evolution periods τ_{sum}.
Overall, the experiments performed with the 500 μM solution affirm the approximation made in Eq. (12). One could in principle refine the approximation and include a constant multiplication factor that includes dipolar attenuation, as observed here experimentally. However, the analysis of experimental data is not sensitive to such a constant multiplication factor. The critical criterion for nDEER is the curvature of $B(t)$, which needs
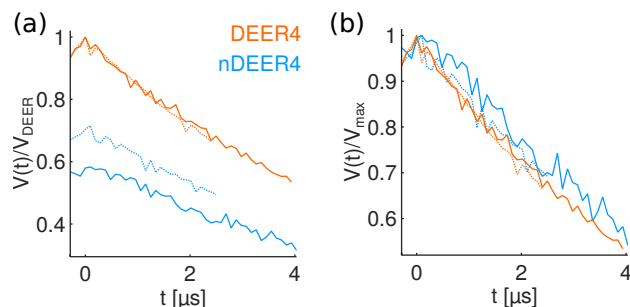

Figure S3: Comparison of inter-molecular background for DEER4 (orange) and nDEER4 (blue) using a 500 μM TEMPOL solution. The delay τ_1 was set to 400 ns. For the delay τ_2, we used τ_2 = 2.5 μs (dashed curves) and τ_2 = 4 μs (solid curves). The time axis t of nDEER4 data was adjusted according to the zero time. (a) Primary data that was normalized to the maximum of the corresponding DEER4 trace. (b) Primary data where each trace was normalized by its maximum value.

to be small enough to avoid significant broadening of the intra-molecular dipolar spectrum.

5. Quantification of pulse skipping artifacts

In the following, the correction of the phase jumps as well as additional artifacts related to pulse skipping are discussed. To correct for the phase jumps, we use the analogous phase estimation as in DeerAnalysis [14], but for two separate data regions. Accordingly, we evaluate

$$\phi_{corr} = \arg\min_{\phi} \sum \text{Im}\{V(t) \cdot e^{i\phi}\}^2 \qquad (13)$$

where the sum only includes the data points that belong to the same region. The assignment of each point to one of the two regions is based on whether an even or an odd number of refocusing pulses precedes a particular time point t.
Since the primary CP2-nDEER and CP4-nDEER data feature pronounced dipolar modulations, we first analyze data originating from the spectral impurity due to E' centers in the sample tube. The data were obtained by using the same experimental dataset as presented in Fig. 4 in the main text, just with a different integration window. The results are shown in Fig. S4, where nDEER4, CP2-nDEER and CP4-nDEER data are indicated in blue, green and magenta, respectively. The small inset on the top shows the spectral integration range to isolate the contribution of the impurity. The upper plot shows the real component of phase corrected primary data, while the middle plot shows the imaginary component. The lower plot shows the difference between normalized CP2-nDEER and CP4-nDEER data, with and without an additional 2 MHz low-pass filter (see also caption).
In order to verify the correction of the abrupt phase jumps in primary data, the imaginary component is of interest. Indeed, there are no residual steps seen that are larger than the noise level. The correction of phase jumps therefore works rather well.
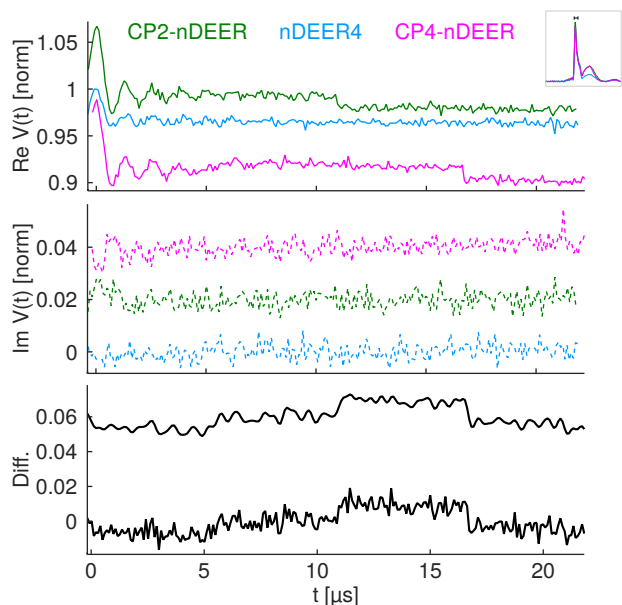
Figure S4: Quantification of pulse skipping artifacts by comparing nDEER signals recorded concurrently with the E' impurity in the sample tube. Accordingly, the FT spectrum of the echo was integrated from -35 MHz to -20 MHz. This integration range is indicated by the black ruler in the small inset on the top right, where echo spectra at $t = 0$ are shown. (see also Fig. 2c in the main text). **Top:** Real component of nDEER4 (blue), CP2-nDEER (green) and CP4-nDEER (magenta) signals after automatic phase correction described in the text. All data are normalized to the nDEER4 echo amplitude. **Middle:** Imaginary component of data in upper plot with vertical displacement of 0.02. **Bottom:** Difference between CP4-nDEER and CP2-nDEER signals, where the lower curve is the difference between the data in the top plot, each normalized by its maximum value. The upper curve displaced at an offset of 0.06 is the difference between signals that were additionally conditioned by a 2 MHz low-pass filter.
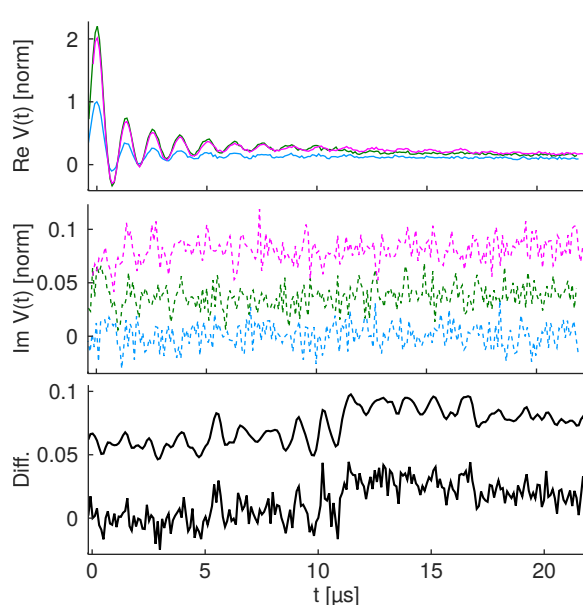
Figure S5: Quantification of pulse skipping artifacts by comparing nDEER signals upon automatic phase correction. **Top:** Real component of nDEER4 (blue), CP2-nDEER (green) and CP4-nDEER (magenta) signals after automatic phase correction described in the text. All data are normalized to the nDEER4 echo amplitude. **Middle:** Imaginary component of data in upper plot with vertical displacement of 0.04. **Bottom:** Difference between CP4-nDEER and CP2-nDEER signals, where the lower curve is the difference between the data in the top plot, each normalized by its maximum value. The upper curve displaced at an offset of 0.06 is the difference between signals that were additionally conditioned by a 2 MHz low-pass filter.

However, the real component displays abrupt discontinuities beyond the noise level. For CP2-nDEER, such a discontinuity is observed around $t = 12$ μs, whereas for CP4-nDEER a similar step is observed around $t = 17$ μs. The relative amplitude of these steps can be inferred from the bottom plot. Notice that these jumps are not related to the phase correction. Rather, these indicate that besides the phase jumps due to the Bloch-Siegert phase shift, there is another effect that results in different echo amplitudes. We currently do not understand the origin of these amplitude jumps. In principle, these could origin from either spin dynamics or instrumentation.

With respect to instrumentation, we note that we kept the power amplifier switched on throughout all pulses and only switched it off after the last pulse. If we would gate the amplifier for each pulse individually and switch it off in-between pulses, we would actually expect rather pronounced artifacts when refocusing pulses are being skipped. Keeping the amplifier open during the entire pulse train is therefore the best suited strategy for experiments with pulse skipping. As mentioned in the main text in Section 2.2, this causes amplifier gating limitations on our spectrometer, if a long sequence requires a gate longer than

54 μs. For CP4-nDEER, for instance, the maximum accessible time window is 31 μs. It may be possible to extend this accessible time window close to 50 μs by gating all pulses up to and including the pump pulse within one single gate, while using separate gates for all pulses after the pump pulse.

Phase-corrected data related to the nitroxide spin labels are shown in Fig. S5 and presented in the same way as in Fig. S4. A successful correction of phase jumps is directly evident when considering the imaginary component, where no discontinuities beyond the noise level are observed. Residual amplitude jumps in the real component are not as easily recognized as for the E' impurity due to the dipolar modulation. However, the difference in the bottom plot reveals that there were also here residual amplitude jumps. Note that besides residual amplitude offsets, the difference also reveals residual modulations, which will be analyzed further below in Section 7 in this SI.

When comparing the difference obtained for the E' impurity and for the nitroxide labels, we observe that the steps had different relative intensities. In particular, the steps around $t = 12$ μs and $t = 17$ μs were of similar height in Fig. S4, if not even slightly larger for the pronounced CP4-nDEER step at $t = 17$ μs. In Fig. S5, this situation is opposite, in particular, the step around $t = 12$ μs related to CP2-nDEER was almost twice as large as the step around $t = 17$ μs related to CP4-nDEER. The enhanced step in CP2-nDEER is even readily observed in the

real components. In particular, the CP2-nDEER trace is always larger than the CP4-nDEER trace for the first half, but becomes attenuated below the CP4-nDEER trace in the second half. Due to the large step beyond the noise level in CP2-nDEER, we corrected the second half by an amplitude scaling. Here, we applied an amplitude scaling by 1.3, which we found by trial-and-error. Notably, this amplitude scaling of the second half removed the significant amplitude jump in the middle of all CP2-nDEER data that we recorded. These include data shown below in Fig. S7 as well as CP2-nDEER data where the inter-pulse delay τ was reduced by a factor of two (data not shown). For CP4-nDEER data, we applied no further correction other than the phase correction, since the amplitude jumps in CP4-nDEER were comparable to the noise level.

With respect to nDEER experiments on other samples, one must therefore be aware of the possibility of amplitude jumps of yet unknown origin. Here, we could characterize and correct these jumps by comparing CP2-nDEER and CP4-nDEER data. Clearly, this is not an option for routine applications. Importantly, we could easily identify the pronounced step in CP2-nDEER by loading the data into DeerAnalysis 2016 and looking at the residual with respect to a regularized fit. Phase-corrected CP2-nDEER and CP4-nDEER data can therefore be checked for residual amplitude steps beyond the noise level by data analysis using established data evaluation tools. If this procedure does not reveal an amplitude step, it means that steps are below the noise level and do not need to be corrected for.

6. Spurious dipolar pathways

As mentioned in the main text, there is some chance on the order of 2% - 4% for the refocusing pulse to not invert a pumped spin. This gives rise to a number of spurious evolution pathways, which is an analogous situation to DEER with multiple pump pulses [15–17]. With I being the inversion efficiency of one refocusing pulse, the weighting factors of the pathways are readily obtained. In particular, the intended nDEER evolution pathway when using N refocusing pulses has a weighting factor of I^N. Spurious pathways where one of the pulses is not flipping the pumped spins have a weighting factor $(1 - I) \cdot I^{N-1}$. More generally, for spurious pathways where n_{sel} out of N refocusing pulses do not flip the pumped spins, the weighting factor is $(1 - I)^{n_{\text{sel}}} \cdot I^{N-n_{\text{sel}}}$.

The dipolar evolution pathways for $n_{\text{sel}} = 0$ up to $n_{\text{sel}} = 2$ for CP2-nDEER and CP4-nDEER are determined in Fig. S6 using the geometrical construction explained in Section 1 of this SI. In particular, each non-sective refocusing pulse is indicated by a filled black circle $\bullet$, while each selective pulse that does not invert the pumped spins is indicated by an empty black circle $\circ$. The crossing point between the forward (black) and backward (red) evolution pathway determines the position of the pump pulse for dipolar refocusing, which is indicated by a red circle $\circ$. Note that for the more elaborate pulse sequences studied here, there may be more than one crossing point between the forward and the backward path. In these cases, the backward path has been continued beyond the first crossing point using transparent red. Moreover, if the forward path already achieves
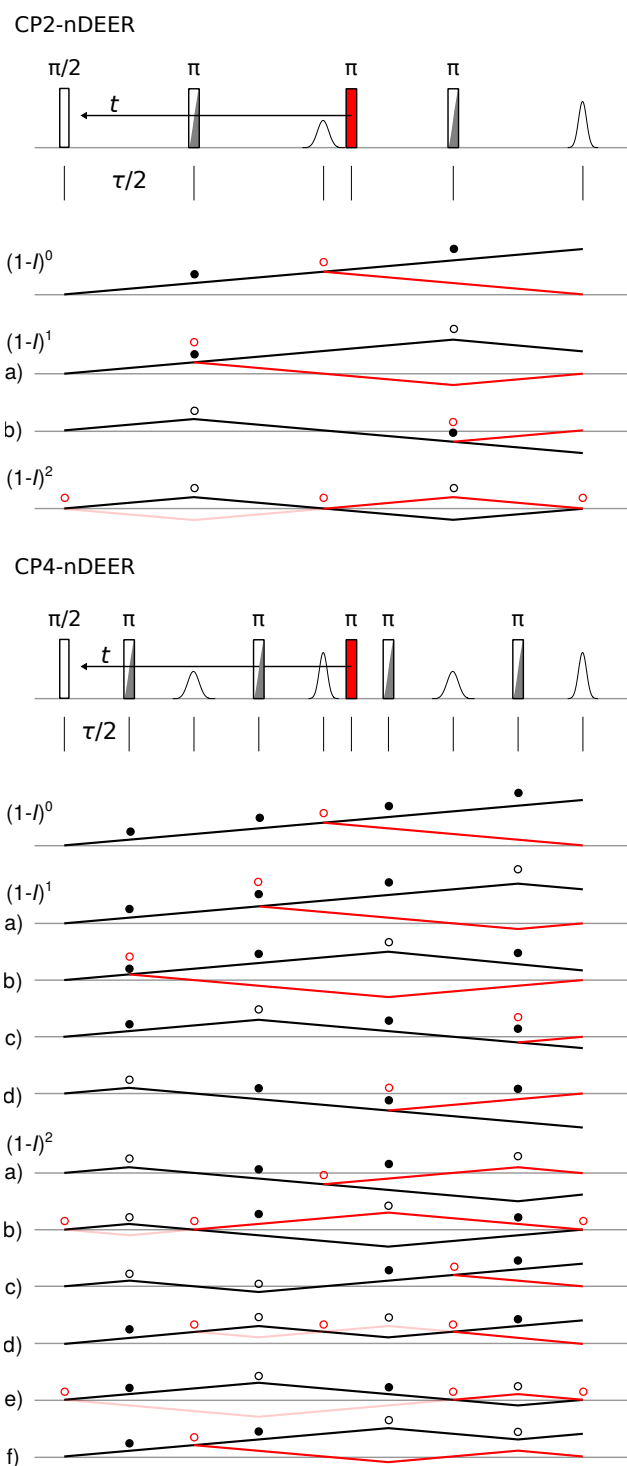

Figure S6: Pictorial representation of dipolar evolution pathways in CP2-nDEER (top) and CP4-nDEER (bottom) for different orders of pulse imperfections $(1 - I)^{n_{\text{sel}}}$ up to $n_{\text{sel}} = 2$. Filled black circles $\bullet$ denote non-selective refocusing, while empty black circles $\circ$ denote selective refocusing. The evolution pathways in black are obtained in absence of the pump pulse. The red curves branching off are due to the pump pulse with timing indicated by the empty red circle $\circ$. All pathways in red refocus the dipolar evolution at the position of the relevant echo.

dipolar refocusing, this corresponds to a crossing point at the position of the echo.

We are solely interested in the zero times of the modulated contributions, which correspond to the positions of the empty red circles. If the pump pulse crosses any of these points, an artificial modulation pathway refocuses and deteriorates data quality with the corresponding weighting factor.

In the experimental data presented in the main text, it is possible to identify some of the spurious pathways with $n_{sel} = 1$ by comparison of adjacent modulation peaks. In order to make these positions more apparent, we present in Fig. S7 a series of nDEER experiments where the flip angle of the refocusing pulses have been reduced deliberately. In particular, we recorded nDEER data with the adiabaticity Q_{crit} of the refocusing pulses set to [1, 2, 4, 8], where the latter corresponds to the data shown in the main text.

For the depicted CP2-nDEER curves, it is clearly seen how the $n_{sel} = 1$ artifact at the middle of the trace gains in amplitude. In addition to that, the worst dataset with $Q_{crit} = 1$ also reveals the $n_{sel} = 2$ artifact that refocuses at the very end of the time axis t. Similarly for the CP4-nDEER curves, the two $n_{sel} = 1$ artifacts

at $t = 6$ μs and at $t = 17$ μs are readily identified. The rather pronounced artifact at the middle of the trace is a superposition of three $n_{sel} = 2$ artifacts. Moreover, the two $n_{sel} = 2$ modulation pathways refocusing at the very end can also be seen.

The nDEER4 series illustrated on top serves as a reference. The only spurious pathway that can be identified here refocuses at the very end. In principle, one would expect two $n_{sel} = 1$ pathways that each refocus at the position of one of the two non-selective refocusing pulses. Accordingly, this explains the modulation at the very end. Moreover, the $n_{sel} = 2$ spurious pathway in nDEER4 is the DEER4 pathway (and vice versa).

As already mentioned, some of the spurious nDEER pathways can be identified in Fig. 4b in the main text. It is worth noting that the largest artifact in the data presented there is seen in DEER4, since spectral overlap between pump and observer pulses results in similar artifacts [19]. In particular, this spurious modulation is due to the second refocusing pulse also flipping the pumped spins. Since the data in Fig. 4b were corrected by division with the background curvature, this artifact at the end of the trace experienced more enhancement during data processing than other spurious pathways.
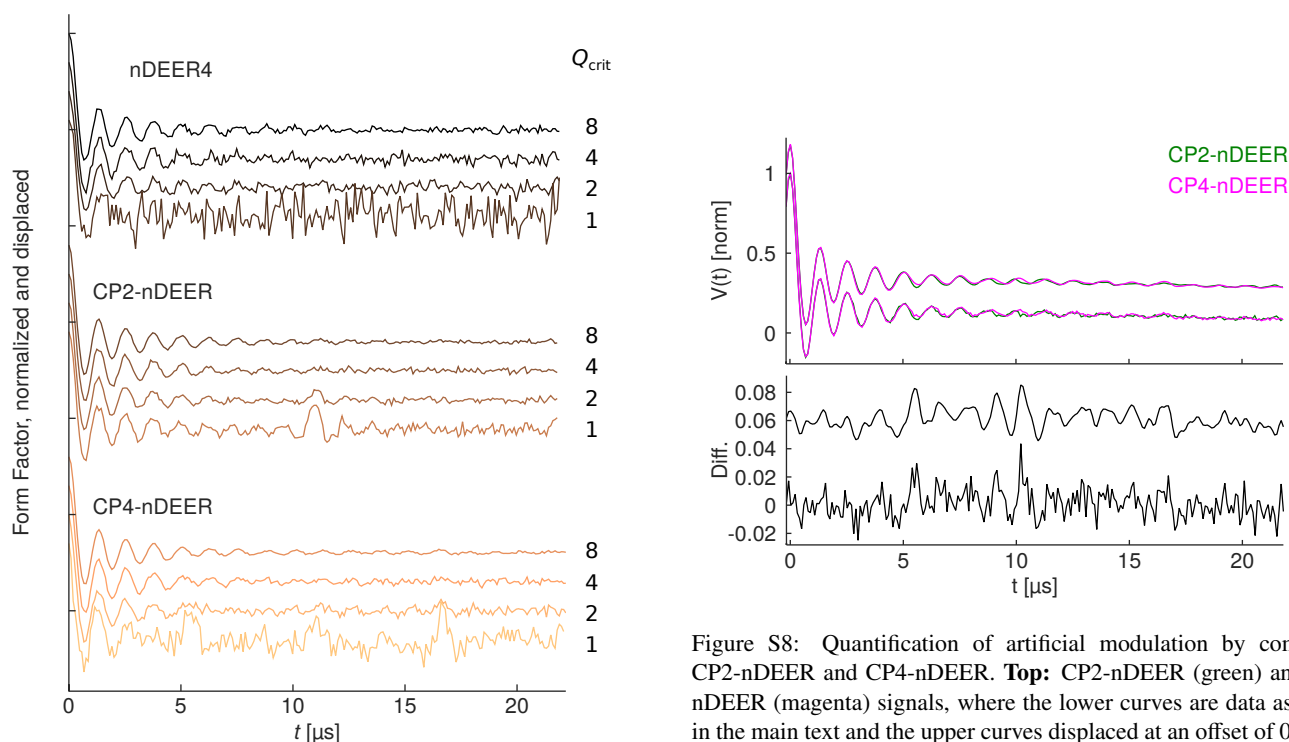

Figure S7: Experimental demonstration of spurious dipolar pathways by reduction of the refocusing pulse's adiabaticity Q_{crit} for nDEER4 (top), CP2-nDEER (middle), and CP4-nDEER (bottom). Data with $Q_{crit} = 8$ corresponds to data shown in the main text acquired with 27 averages. All data at reduced Q_{crit} were acquired with 10 averages. The adiabaticity was varied by reducing the amplitude of the refocusing pulses, where field amplitudes inside the resonator were calibrated using nutation experiments [18]. All form factors were obtained by automatic background fitting within DeerAnalysis 2016 [14] and were rescaled for identical modulation depths.

Figure S8: Quantification of artificial modulation by comparing CP2-nDEER and CP4-nDEER. **Top:** CP2-nDEER (green) and CP4-nDEER (magenta) signals, where the lower curves are data as shown in the main text and the upper curves displaced at an offset of 0.2 were conditioned by a low-pass filter. A second-order Butterworth lowpass with 2 MHz cutoff was applied in forward and reverse direction to compensate for delays (*filtfilt* command of MATLAB^{TM} signal processing toolbox). All data are normalized by their maximum value at $t = 0$. **Bottom:** Difference between CP4-nDEER and CP2-nDEER signals, where the lower curve is the difference between the data as showed in the main text and the upper curve displaced at an offset of 0.06 is the difference between the filtered data. The ordinate is the difference with the same normalized units as in the upper figure. This difference therefore needs be compared to nDEER modulation depths of 0.86 and 0.87 for CP2-nDEER and CP4-nDEER, respectively.

7. Quantification of spurious dipolar modulation

Since the spurious dipolar modulation pathways are difficult to observe in primary data, we here quantify the modulation depth of these pathways for further reference on the performance of nDEER. We found that such a quantification works best when comparing CP2-nDEER and CP4-nDEER data, since the primary data of the two experiments had best alignment of their time axes t.

The upper plot in Fig S8 shows normalized CP2-nDEER (green) and CP4-nDEER (magenta) signals, where the lower set of curves corresponds to primary data and the upper set to data conditioned by a low-pass filter. The lower plot shows the difference between CP2-nDEER and CP4-nDEER, again with and without filtering. Note that as compared to the bottom plot in Fig. S5, the pronounced amplitude step due to nDEER2 is no longer present because of the amplitude correction described above in Section 5 of this SI.

In the difference signal, it can be seen that the primary data agree within the range [-0.025, 0.044], including noise. By suppressing noise using low-pass filtering, the agreement is within [-0.014, 0.025]. The CP4-nDEER artifacts for $n_{sel} = 1$ at $t = 6$ μs and at $t = 17$ μs are readily recognized. Moreover, the $n_{sel} = 1$ artifact of CP2-nDEER corresponds to the negative peak at $t = 11$ μs in the difference signal. Within the uncertainty of our data, we can estimate the spurious modulation to be below 3%. As compared to the modulation strength of the principal nDEER oscillation of 86%, this corresponds to a net contamination by 3.5%. This means that with our nDEER performance, spurious pathways have a modulation depth of only 3.5% of the modulation depth of the principal signal.

In yet unpublished results, the performance of five-pulse DEER with selective monochromatic refocusing [15] has been optimized using the same model compound both at X band and at Q band. The Q-band performance on the same spectrometer was significantly worse than the nDEER performance reported in this study. Only at X band, where we observed better agreement between experimental and theoretical pulse performance, the suppression of spurious modulations came close to nDEER.

8. Echo decays for nDEER and DEER

As mentioned in the main text, the efficiency of the refocusing pulses is critical in determining how well the improved dynamical decoupling for $N > 2$ can be utilized. To point at the benefit of non-selective refocusing pulses in this respect, echo decays for both selective and non-selective refocusing are compared.

The results are shown in Fig. S9, where the upper set of curves illustrates the decay of the nDEER4 (blue), CP2-nDEER (green), and CP4-nDEER (magenta) echo as a function of the sequence duration t_{echo}. This set of curves corresponds to the data shown in Fig. 5a in the main text. These decays were therefore recorded with the pump pulse at the position where the dipolar coupling refocused.

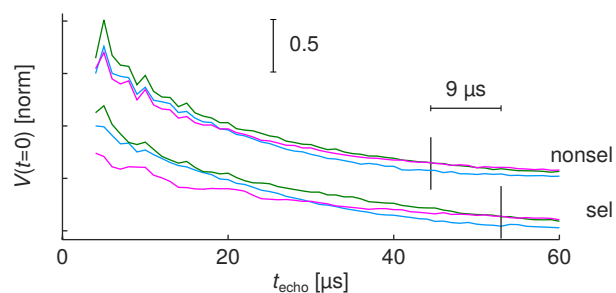The lower set of curves were recorded by substitution of all

Figure S9: Comparison of nDEER and DEER echo decays, where t_{echo} is the time between the first $\pi/2$ pulse and the detected echo. The uppper set of curves corresponds to $V(t = 0)$ of nDEER4 (blue), CP2-nDEER (green), and CP4-nDEER (magenta), as also shown in the main text. The lower set of curves show experiments with the same timing as the corresonding nDEER sequences, but using selective monochromatic refocusing pulses with 12 ns duration. There was no pump pulse with selective refocusing. The black vertical lines denote the crossover points, where refocusing with 4 pulses becomes more effective than refocusing with 2 pulses.

chirp refocusing pulses by monochromatic pulses at the observation frequency. With this substitution, the pump pulse was no longer needed to achieve dipolar refocusing. Each of the two sets of curves was normalized by the first point of the blue curve and the two sets were vertically displaced by 0.5. For both type of experiments, the change from a DEER-like pulse spacing to a CP pulse train with $N = 2$ resulted in a strictly larger echo amplitude. For $N = 4$ refocusing pulses, however, two refocusing pulses are added, which resulted in a larger relative loss for the monochromatic pulses as compared to the chirp pulses. The crossing point where the improved dynamical decoupling of the $N = 4$ pulse train compensates for the initial amplitude loss with respect to the $N = 2$ pulse train therefore shifted to a later time t_{echo}. For ease of visualization, we indicated the approximate crossing points by the black vertical lines. The time shift between these two vertical lines is 9 μs.

Note that we are here solely discussing the relative improvement when going from $N = 2$ to $N = 4$ refocusing pulses. The fact that non-selective chirp refocusing results in an absolute improvement due to the larger echo bandwidth has been discussed in the main text.

References

[1] R. Freeman, S. P. Kempsell, M. H. Levitt, Broadband decoupling and scaling of heteronuclear spin-spin interactions in high-resolution NMR, J. Magn. Reson. 35 (1979) 447 – 450.

[2] E. Kupĉe, R. Freeman, Compensation for spinspin coupling effects during adiabatic pulses, J. Magn. Reson. 127 (1997) 36 – 48.

[3] V. V. Kurshev, A. M. Raitsimring, Y. D. Tsvetkov, Selection of dipolar interaction by the 2 + 1 pulse train ESE, J. Magn. Reson. 81 (1989) 441 – 454.

[4] O. Sørensen, G. Eich, M. H. Levitt, G. Bodenhausen, R. Ernst, Product operator formalism for the description of NMR pulse experiments, Prog. Nucl. Magn. Reson. Spectrosc. 16 (1984) 163–192.

Supplementary Information

[5] G. Jeschke, M. Pannier, A. Godt, H. Spiess, Dipolar spectroscopy and spin alignment in electron paramagnetic resonance, Chem. Phys. Lett. 331 (2000) 243 – 252.

[6] P. P. Borbat, J. H. Freed, Multiple-quantum ESR and distance measurements, Chem. Phys. Lett. 313 (1999) 145 – 154.

[7] G. Jeschke, S. Pribitzer, A. Doll, Coherence transfer by passage pulses in electron paramagnetic resonance spectroscopy, J. Phys. Chem. B 119 (2015) 13570–13582.

[8] A. Doll, G. Jeschke, EPR-correlated dipolar spectroscopy by Q-band chirp SIFTER, Phys. Chem. Chem. Phys. 18 (2016) 23111–23120.

[9] A. Doll, S. Pribitzer, R. Tschaggelar, G. Jeschke, Adiabatic and fast passage ultra-wideband inversion in pulsed EPR, J. Magn. Reson. 230 (2013) 27 – 39.

[10] R. G. Larsen, D. J. Singel, Double electron–electron resonance spin–echo modulation: Spectroscopic measurement of electron spin pair separations in orientationally disordered solids, J. Chem. Phys. 98 (1993) 5134–5146.

[11] A. D. Milov, Y. D. Tsvetkov, Double electron-electron resonance in electron spin echo: Conformations of spin-labeled poly-4-vinilpyridine in glassy solutions, Appl. Magn. Reson. 12 (1997) 495–504.

[12] D. R. Kattnig, J. Reichenwallner, D. Hinderberger, Modeling excluded volume effects for the faithful description of the background signal in double electron-electron resonance, J. Phys. Chem. B 117 (2013) 16542–16557.

[13] G. Jeschke, Dipolar spectroscopy - double-resonance methods, eMagRes 5 (2016) 1–18.

[14] G. Jeschke, V. Chechik, P. Ionita, A. Godt, H. Zimmermann, J. Banham, C. Timmel, D. Hilger, H. Jung, DeerAnalysis2006 - a comprehensive software package for analyzing pulsed ELDOR data, Appl. Magn. Reson. 30 (2006) 473–498.

[15] P. P. Borbat, E. R. Georgieva, J. H. Freed, Improved sensitivity for long-distance measurements in biomolecules: Five-pulse double electron-electron resonance, J. Phys. Chem. Lett. 4 (2013) 170–175.

[16] P. E. Spindler, S. J. Glaser, T. E. Skinner, T. F. Prisner, Broadband inversion PELDOR spectroscopy with partially adiabatic shaped pulses, Angew. Chem. Int. Ed. 52 (2013) 3425–3429.

[17] P. E. Spindler, I. Waclawska, B. Endeward, J. Plackmeyer, C. Ziegler, T. F. Prisner, Carr-purcell pulsed electron double resonance with shaped inversion pulses, J. Phys. Chem. Lett. 6 (2015) 4331–4335.

[18] A. Doll, G. Jeschke, Fourier-transform electron spin resonance with bandwidth-compensated chirp pulses, J. Magn. Reson. 246 (2014) 18 – 26.

[19] K. Salikhov, I. Khairuzhdinov, Four-pulse ELDOR theory of the spin 1/2 label pairs extended to overlapping EPR spectra and to overlapping pump and observer excitation bands, Appl. Magn. Reson. 46 (2015) 67–83.